Accepted Manuscript

Facile synthesis of NiAl layered double hydroxide nanoplates for high-performance asymmetric supercapacitor

Lei Li, Kwan San Hui, Kwun Nam Hui, Qixun Xia, Jianjian Fu, Young-Rae Cho

Please cite this article as: L. Li, K.S. Hui, K.N. Hui, Q. Xia, J. Fu, Y.-R. Cho, Facile synthesis of NiAl layered double hydroxide nanoplates for high-performance asymmetric supercapacitor, *Journal of Alloys and Compounds* (2017), doi: 10.1016/j.jallcom.2017.06.062.

This is a PDF file of an unedited manuscript that has been accepted for publication. As a service to our customers we are providing this early version of the manuscript. The manuscript will undergo copyediting, typesetting, and review of the resulting proof before it is published in its final form. Please note that during the production process errors may be discovered which could affect the content, and all legal disclaimers that apply to the journal pertain.

Facile synthesis of NiAl layered double hydroxide nanoplates for high-performance asymmetric supercapacitor

Lei Li [a], Kwan San Hui [b*], Kwun Nam Hui [c**], Qixun Xia[a], Jianjian Fu[a] and Young-Rae Cho [a***]

[a]School of Materials Science and Engineering, Pusan National University, San 30 Jangjeon-dong, Geumjeong-gu, Busan 609-735, Republic of Korea

[b]School of Mathematics, University of East Anglia, Norwich, NR4 7TJ, United Kingdom

[c]Institute of Applied Physics and Materials Engineering, University of Macau, Avenida da Universidade, Macau, China

Corresponding author:

E-mail: k.hui@uea.ac.uk *(Kwan San Hui)*

Tel: +82 2-2220-0441; Fax: +82 2-2220-2299

E-mail: bizhui@umac.mo *(Kwun Nam Hui)*

Tel: +853 8822-4426; Fax: +853 8822-2426

E-mail: yescho@pusan.ac.kr *(Y. R. Cho)*

Tel.: +82 051-510-2389; Fax: +82 5-1514-4457

1   **Abstract**

2   Layered double hydroxide (LDH) is a promising electrode material for supercapacitor

3   owing to its versatility in compositions, high theoretical capacitance, environmental

4   benignity, and low cost. However, capacity fading of LDH hinders its application in

5   energy storage. Herein, we develop a facile approach to synthesize NiAl-LDH

6   nanoplates possessing high electrochemical activity and desirable morphology to

7   improve ion diffusion kinetics and reduce charge transfer resistance, leading to

8   enhanced specific capacitance compared to pristine NiAl-LDH. Scanning electron

9   microscopy shows that the LDH nanoplates are as thin as ~30 nm with a mean lateral

10   dimension of ~150 nm. The NiAl-LDH nanoplates electrode delivers remarkably high

11   specific capacitance of 1713.2 F g^{-1} at 1 A g^{-1} and good cycling ability of 88%

12   capacitance retention over 5000 cycles compared to only 757.1 F g^{-1} at 1 A g^{-1} and

13   76.4% of the pristine NiAl-LDH. An asymmetric supercapacitor (ASC) is assembled

14   using NiAl-LDH nanoplates and graphene as positive and negative electrodes,

15   respectively. The ASC operating at 1.4 V delivers a high specific capacitance of 125 F

16   g^{-1} at 1 A g^{-1} with a high energy density of 34.1 Wh kg^{-1} at a power density of 700 W

17   kg^{-1} and outstanding cyclic stability (91.8% capacitance retention after 5000 cycles).

18

19   **KEYWORDS:** layered double hydroxide; nanoplates; ultrathin; graphene;

20   asymmetric supercapacitor

21

22   **Introduction**

23   Supercapacitors, that includes electric double-layer capacitors (EDLCs, generally composed

24   of carbonaceous materials) based on electrostatic adsorption/desorption, and

1 pseudocapacitors (such as in transition metal oxides/hydroxides) based on Faradaic reactions,

2 are advantageous for their high power density, fast charge propagation dynamics, and long

3 cycle life compared with batteries [1-5]. In the electrochemical field, layered double

4 hydroxide (LDH), layered materials, which is composed of brucite-like host layers and

5 charge-compensating interlayer anions, has attracted a great deal of attention because of their

6 high redox activity, relatively low cost, and environmentally friendly features [6-8]. The

7 general formula of LDHs can be described as $[M_{1-x}^{2+}M_x^{3+}(OH)_2](A^{n-})_{x/n}\cdot mH_2O$, where M^{2+}

8 indicates divalent cation (Ni^{2+}, Co^{2+}, Cu^{2+}, Zn^{2+}, Mg^{2+}, etc.), M^{3+} indicates trivalent cation

9 (Al^{3+}, Mn^{3+}, Cr^{3+}, Fe^{3+}, etc.), and A^{n-} indicates interlayer exchangeable anion (OH^-, SO^{4-},

10 NO^{3-}, etc.) [9, 10]. As a result, electrical double-layer capacitance can be obtained by the

11 abundant slabs among the structure, while Faradaic reactions can be achieved at the surface

12 of electroactive sites for charge storage [8, 11, 12]. Theoretically, the specific capacitance is

13 ascribed to the Faradaic redox reaction of Ni(II)/Ni(III) based on eqt 1:[13]

14
$$Ni(OH)_2 + OH^- \leftrightarrow NiOOH + H_2O + e^- \qquad (1)$$

15 Al does not participate in the Faradaic reactions. Hence, the theoretical specific capacitance

16 of NiAl-LDH is contributed from $Ni(OH)_2$ which has a theoretical specific capacitance of

17 2082 F g^{-1} [14]. Therefore, LDH materials hold the great promise in achieving high energy

18 density and power density simultaneously compared to other supercapacitive electrode

19 materials such as NiO [15, 16], Co_3O_4 [17], $NiCo_2O_4$ [18] and $LaNiO_3/NiO$ [19]. However,

20 the low conductivity of LDH that adversely affects the electron transfer kinetics resulting in

21 poor cycling stability and impeding its potential in commercial applications [6, 20-22].

22

23 NiAl-LDH as a distinguish electrode material has been applied in electrochemical

24 fields. In this material, $Ni(OH)_2$ was employed to provide the capacitance (with the

theoretical specific capacitance of 2082 F g^{-1}) [14] and $Al(OH)_3$ was used to support the layered structural. To improve the electrochemical performance of the active materials, nanostructured NiAl-LDH [23, 24] and its hybridization with carbon nanotube [5, 25, 26], and graphene [6, 27, 28] have been extensively investigated and employed in supercapacitors. Among the reported nanostructures, nanoplates have been regarded as a promising morphology in the field of energy storage owing to the short ion diffusion path and abundant electroactive sites on the exposed surface, which is beneficial to achieve high specific capacitance, superior cycling stability, and high-rate capability in supercapacitor devices [11, 29]. Therefore, it is attractive to develop a synthesis route to achieve these essential aspects simultaneously.

Here, we report a facile approach to synthesize NiAl-LDH with desirable nanoplates morphology by facile hydrothermal method (H-NiAl-LDH). For comparison, electrochemical performance of pristine NiAl-LDH synthesized by co-precipitation method (P-NiAl-LDH) was studied. The H-NiAl-LDH nanoplates electrode exhibits a high specific capacitance of 1713.2 F g^{-1} at 1 A g^{-1} and good cycling stability of 88% capacitance retention over 5000 cycles compared to only 757.1 F g^{-1} at 1 A g^{-1} and 76.4% of the pristine NiAl-LDH. An asymmetric supercapacitor made of H-NiAl-LDH//G operated at 1.4 V delivers a high energy density of 34.1 W h kg^{-1} at a power density of 700 W kg^{-1} and excellent cycling stability of 91.8% initial capacitance retention over 5000 cycles.

Experimental

2.1. Raw material

1   Aluminum nitrate nonahydrate ($Al(NO_3)_3 \cdot 9H_2O$), nickel nitrate hexahydrate

2   ($Ni(NO_3)_2 \cdot 6H_2O$) and graphite powder were purchased from Sigma-Aldrich (USA).

3   Sodium hydroxide (NaOH), sodium carbonate (Na_2CO_3) and urea (($NH_2)_2CO$) were

4   purchased from Junsei (Japan). Acetone and anhydrous ethanol were supplied by SK

5   Chemical (Korea). In the experiment process, deionized water was used in washing

6   and synthesis process.

7

8   2.2. NiAl LDH by co-precipitation method

9   Solution A (0.2 M $Ni(NO_3)_2 \cdot 6H_2O$ and 0.1 M $Al(NO_3)_3 \cdot 9H_2O$) and solution B (0.75 M

10 NaOH and 0.2 M Na_2CO_3) were dissolved in 80 mL deionized water separately.

11 Subsequently, solution A and B were mixed slowly and transferred into a three-necked

12 round flask with vigorous stirring at 45 °C for 2 h. Then the mixed solution was placed

13 in a water bath at 60 °C for 12 h. After crystallization process, the products were

14 filtered, washed several times with deionized water and alcohol. Finally, the NiAl-

15 LDH green solid product was dried at 60 °C for 12 h in a vacuum oven.

16

17 2.3. NiAl LDH by hydrothermal method

18 $Ni(NO_3)_2 \cdot 6H_2O$ and $Al(NO_3)_3 \cdot 9H_2O$ were dissolved in 35 mL deionized water with

19 vigorous stirring for 15 min to give solution A. 15 mmol urea was added slowly in

20 solution A and stirring for 15 min to obtain solution B. Solution B was transferred to a

21 50 mL Teflon-lined autoclave, which was sealed and placed in oven at 180 °C for 12 h.

22 After cooling and centrifugation, followed by washing several times with ethanol and

23 water, the NiAl-LDH green solid product was dried at 60 °C for 12 h in a vacuum

24 oven.

1

2   2.4. Materials characterization

3   The powder X-ray diffraction (XRD) was recorded with a Bruker D8 Advance X-ray

4   using Cu Kα radiation (λ = 0.15406 nm) at 40 kV accelerating voltage and a 30 mA

5   current. The samples were scanned at 2θ, from 5° to 70° at scanning speed 5° min^{-1}

6   with a 0.02° step. Scanning electron microscope (SEM) was performed using Hitachi

7   S-4800 with an applied voltage of 5 kV. High-resolution transmission electron

8   microscopy (HRTEM) and selected area electron diffraction (SAED) pattern were

9   measured using JEOL 2100F. The Fourier transform infrared spectroscopy (FTIR) was

10   measured using Bruker Tensor 27 with the KBr self-supported pressing technique.

11   Finely powdered samples (1%) were pressed at 5 ton cm^{-2} to form the flat slices. The

12   samples were scanned with a 2 cm^{-1} resolution between 400 and 4000 cm^{-1} at the

13   scanning time 32 s. The Brunauer-Emmett-Teller (BET) surface area and pore size

14   distributions were characterized using a Micromeritics 3Flex analyzer at liquid

15   nitrogen temperature of 77 K °C. Before the experiments, the samples were degassed

16   in a vacuum oven at 60 °C for 12 h.

17

18   2.5. Electrochemical measurements

19   The electrochemical tests were conducted on an IVIUM nstat electrochemical station

20   based on our previous setting . The working electrodes were prepared by mixing the

21   active material (5 mg), acetylene black, and polytetrafluorene-ethylene (PTFE) binder

22   at a weight ratio of 80:15:5 and dispersing the mixture in ethanol to produce a

23   homogeneous paste. The mixture was carefully placed onto nickel foam (1 cm×1

24   cm×0.2 cm), and then dried in a vacuum oven at 80 °C before pressing under a

1 pressure of 20 MPa. The three-electrode tests were carried out with saturated calomel

2 electrode (SCE, Hg/Hg_2Cl_2) as the reference electrode and platinum foil as the counter

3 electrode. The electrolyte was a 6.0 M KOH aqueous solution. The galvanostatic

4 charge/discharge curves were measured at different current densities. The EIS

5 measurements were carried out from 100 kHz to 0.01 Hz at the open circuit potential

6 with an AC perturbation of 5 mV. The specific capacitance (C_s) of P-NiAl-LDH and

7 H-NiAl-LDH electrodes were calculated from the galvanostatic charge/discharge

8 curves as follows:

9 $$C_s = I \times \Delta t/(m \times \Delta V) \tag{2}$$

10 where I is the discharge current (A), Δt is the discharge time (s), m is the mass of the

11 electroactive material in the electrode (g), and ΔV is the total potential deviation (V).

12 The C_s of ASC was calculated from the galvanostatic charge/discharge curves as

13 follows:

14 $$C_s = I \times \Delta t/(m' \times \Delta V) \tag{3}$$

15 where m' is the total mass (LDH: 2.86 mg, GNS: 14.53 mg) of electroactive materials

16 in the positive and negative electrodes (g). The energy and power densities of the

17 asymmetric supercapacitor were calculated as follows:

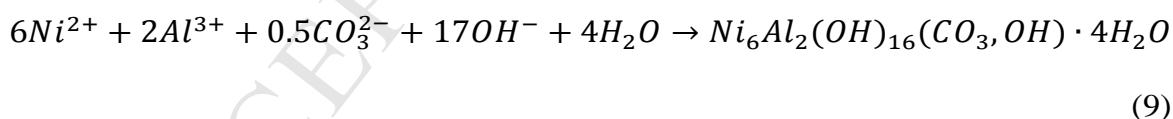18 $$E = 0.5 \times C_s \times V^2 \tag{4}$$
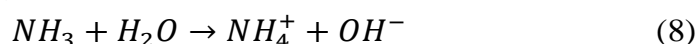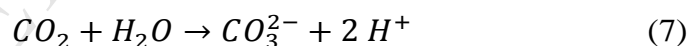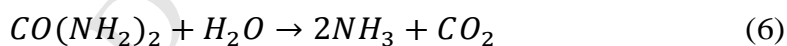
19 $$P = E/\Delta t \tag{5}$$

20 where E (Wh kg^{-1}) is the energy density, V (V) is the cell voltage excluding the IR

21 drop, P (W kg^{-1}) is the average power density, and Δt is the discharge time.

22

23 **Results and discussion**

24 3.1. Material characterization

Fig. 1a shows the typical X-ray diffraction (XRD) patterns of the P-NiAl-LDH and H-NiAl-LDH. The well-defined diffraction peaks observed at 11.7°, 23.5°, 35.2°, 61.4°, and 75.4° 2θ were indexed to (003), (006), (012), (110), and (205) planes, respectively, matching well with hydrotalcite-like NiAl-LDH structure (JCPDS 15-0087) [6], indicating the synthesized materials correspond to both $Ni(OH)_2$ and $Al(OH)_3$. Results show that the peak intensity of H-NiAl-LDH is higher than that of P-NiAl-LDH, indicating a higher degree of crystallinity. The growth mechanism of NiAl LDH nanoplates follows a preferred orientation growth process [30]. In the hydrothermal process, the slow hydrolysis of urea leads to in situ release of OH^- and, CO_3^{2-} (eqt 6-8), which further initiates the precipitation of Ni^{2+} and Al^{3+} to form aluminum aquohydroxo complexes and nickel hydroxides (eqt 9) [31]. Consequently, nickel/aluminum salts are converted to NiAl LDHs nanoplates by olation reactions and crystallization [23].

$$CO(NH_2)_2 + H_2O \rightarrow 2NH_3 + CO_2 \qquad (6)$$

$$CO_2 + H_2O \rightarrow CO_3^{2-} + 2H^+ \qquad (7)$$

$$NH_3 + H_2O \rightarrow NH_4^+ + OH^- \qquad (8)$$

$$6Ni^{2+} + 2Al^{3+} + 0.5CO_3^{2-} + 17OH^- + 4H_2O \rightarrow Ni_6Al_2(OH)_{16}(CO_3,OH) \cdot 4H_2O$$

$$(9)$$

The FT-IR spectra of P-NiAl-LDH and H-NiAl-LDH are shown in Fig. 1b. Broad peaks at 3354 cm^{-1} and 3443 cm^{-1}, respectively, are attributed to the hydroxyl (O-H) stretching vibration of water molecules in the hydrogen-bonded OH groups and the interlayer, accompanied with the bending mode at 1632 cm^{-1} and 1651 cm^{-1} [32]. The strong absorption peaks at 1356 cm^{-1} and 1360 cm^{-1} are due to the interlayer anion (CO_3^{2-}) from sodium carbonate and urea hydrolysis during the co-precipitation and

1   hydrothermal procedure [33]. In addition, the stretching modes and metal oxygen (M-

2   O) bending in the brucite-like lattice are associated with the absorption bands below

3   800 cm^{-1} [34]. Results clearly indicate that LDH sample synthesized by hydrothermal

4   method resulting in stronger absorption peaks compared with co-precipitation method,

5   suggesting the hydrothermal method resulting in higher quality of materials.

6

7   To investigate the surface morphology, field-emission scanning electron microscopy

8   (FESEM) images of the as-obtained NiAl-LDH samples by different synthetic

9   methods are shown in Fig. 2. Fig. 2a shows the P-NiAl-LDH samples are particle-like

10   without a definite shape and the mean size is determined to be ~ 5 µm. SEM image

11   clearly reveals that the P-NiAl-LDH samples aggregate the layers of LDH of all sizes

12   and grow in different directions, which hinders the ion diffusion [6]. In contrast, H-

13   NiAl-LDH samples show distinct hexagonal nanoplates with a mean lateral dimension

14   of 150 nm and thickness as thin as 30 nm (Figs. 2c and d). Such nanoplates

15   morphology of H-NiAl-LDH is expected to provide more electroactive sites for redox

16   reaction and decrease the ion diffusion pathways, and thus enhance the specific

17   capacitance. TEM was further performed to investigate the microstructure of H-NiAl-

18   LDH. High-resolution TEM image (Fig. 2e) shows that H-NiAl-LDH possesses a thin

19   nanoplate feature with an average diameter of ~100 nm, which is beneficial to achieve

20   high specific capacitance owing to an efficient and rapid diffusion of electrolyte ions

21   to the active material surface [35]. Lattice fringes with an equal interplanar distance of

22   0.224 and 0.125 nm that are indexed to (015) and (205) confirmed the polycrystalline

23   phases of hydrotalcite-like structure (Fig. 2f) [8]. Inset of Fig. 2f shows the

24   corresponding selected area electron diffraction (SAED) pattern of the nanoplates,

1   where the diffraction rings were readily indexed to the (015) and (205) planes of the

2   NiAl-LDH phase. These results are consistent with the XRD patterns.

3

4   To further affirm the surface area and interconnected pores of the materials, the BET

5   nitrogen adsorption/desorption isotherm and the Barrett-Joyner-Halenda (BJH) pore

6   size distribution curves of P-NiAl-LDH and H-NiAl-LDH were measured and

7   presented in Fig. 3 and Table 1. A typical H2 type hysteresis loop is observed in the P-

8   NiAl-LDH and H-NiAl-LDH curves, suggesting the existence of mesopores in all

9   samples [10]. Fig. 3b shows the pore size distribution (PSD) of P-NiAl-LDH and H-

10 NiAl-LDH samples, revealing the existence of a network of pores with various sizes.

11 The average pore size, BET specific surface area and the corresponding pore volume

12 of P-NiAl-LDH and H-NiAl-LDH, respectively, are 10.64 and 3.55 nm, 26.54 and

13 31.35 $m^2 g^{-1}$, and 0.20 and 0.23 $cm^3 g^{-1}$, respectively. Although the surface of the P-

14 NiAl-LDH samples is composed of smaller particles (Fig. 2b), the particles aggregate

15 together and result in the smaller specific surface area [6]. In contrast, the H-NiAl-

16 LDH samples are nanoplates morphology (Fig. 2bc) that the surfaces of the LDH are

17 highly exposed, which contributes to a higher specific surface area. On the other hand,

18 the P-NiAl-LDH samples display mean pore size of 10.64 nm, which could not

19 provide the effective accessibility of the OH^- to the active LDH materials for efficient

20 redox reactions in electrochemical energy storage applications. [28] In contrast, the H-

21 NiAl-LDH samples show PSD maxima centered at 3.55 nm, which is the most suitable

22 for better OH^- diffusion in electrochemical energy storage applications [36]. In

23 addition, the BET specific surface area and pore volume of the H-NiAl-LDH samples

24 are much higher than those of the P-NiAl-LDH samples, which is attributed to the

1 hexagonal lamellar nanostructure that decreases the aggregation of layers of NiAl-

2 LDH materials. Such a unique porous structure can effectively facilitate ions

3 transports and provide high interfaces between electrolyte ions and electroactive

4 materials during a redox reaction, which is critical for efficient electrochemical

5 reaction.

6

7 3.2. Electrochemical characterization

8 Cyclic voltammetry (CV) and galvanostatic charging/discharging (GCD) tests were

9 conducted to evaluate the electrochemical properties of the obtained NiAl-LDH

10 synthesized by two methods. Fig. 4a shows the CV curves of P-NiAl-LDH and H-

11 NiAl-LDH in a 6 M KOH solution at a scan rate of 10 mV s^{-1} in the voltage range of 0

12 to 0.6 V (vs. SCE). Pairs of redox peaks revealed the occurrence of Faradaic redox

13 reactions between different oxidation states of Ni according to the eqt 1. In general, a

14 better reversibility in the redox reaction attributed to the smaller potential difference

15 between the anodic and cathodic peak potential (ΔE) [28]. As shown in Fig. 4a, the

16 potential difference of the H-NiAl-LDH electrode (ΔE =140 mV) was smaller than P-

17 NiAl-LDH electrode (ΔE =170 mV), which showed better reversibility. This result

18 was due to the H-NiAl-LDH electrode provided a larger surface area to contact the

19 electrolyte, which facilitated the efficient diffusion of OH$^-$ ions during the redox

20 reactions [6, 28]. In addition, the CV curve of H-NiAl-LDH electrode showed larger

21 integrated areas, indicating a higher specific capacitance. CV curves of P-NiAl-LDH

22 (Fig. 4b) and H-NiAl-LDH (Fig. 4c) electrodes at different scan rate 5- 50 mV s^{-1}

23 revealed a well-defined pair of redox peaks at high scan rate, indicating fast ionic

24 diffusion of the electrodes and reversible redox reaction of Ni^{2+}/Ni^{3+} [8]. Increasing

1   the scan rate, the anodic peaks shifted to a more positive potential, whereas the

2   cathodic peaks shifted to a more negative potential, which is ascribed to an increase of

3   internal diffusion resistance of the electrodes [37]. The plot of the cathodic peak

4   current densities against the square root of the scan rate ($v^{1/2}$) of P-NiAl-LDH and H-

5   NiAl-LDH electrodes (Fig. 4d) show a linear response, indicating the Faradaic

6   reaction follows a diffusion-controlled process. Diffusion coefficient (*D*) of OH$^-$ ion

7   in both electrodes is calculated using Randles–Sevcik eqt 11.

8
$$I_p = 2.69 \times 10^5 \times n^{\frac{3}{2}} \times A \times \sqrt{D} \times C \times \sqrt{v} \tag{11}$$

9
$$D(\text{H}-NiAl-LDH)/D(\text{P}-NiAl-LDH) = [(I_p/\sqrt{v})(\text{H}-NiAl-LDH)/(I_p/\sqrt{v})(\text{P}-NiAl-LDH)]^2$$

10
$$= (28.01/19.99)^2 = 1.963 \tag{12}$$

11   where I_p is the peak current, *n* is the number of electrons involved in the reaction, *A* is

12   the surface area of the electrode, *D* is the diffusion coefficient of the electrode

13   material, *C* is the proton concentration, and *v* is the scanning rate. The diffusion

14   coefficient of the H-NiAl-LDH electrode ($D_{\text{H-NiAl-LDH}}$) is around 1.963 times larger

15   than that of the P-NiAl-LDH electrode ($D_{\text{P-NiAl-LDH}}$), showing higher ion mobility

16   could be achieved in H-NiAl-LDH electrode during the electrochemical reaction.

17

18   Fig. 5a shows the discharge measurements of the P-NiAl-LDH and H-NiAl-LDH

19   electrodes were carried out between 0 to 0.38 V at a current density of 1 A g^{-1}. The

20   nonlinear lines discharge curves indicated the pseudo-capacitance behavior attributed

21   to quasi-reversible redox reactions at electrode surface [38]. Fig. 5b and c show

22   discharge measurements of the P-NiAl-LDH and H-NiAl-LDH electrodes at different

23   current densities. The specific capacitances of P-NiAl-LDH electrode were calculated

24   as 757.1, 668.6, 625.7, 594.3 and 571.4 F g^{-1}, whereas the specific capacitances of H-

1 NiAl-LDH electrode were calculated as 1713.2, 1389.5, 1207.8, 1084.2 and 960.5 F g$^-$

2 ^{1} at current densities of 1, 2, 3, 4 and 5 A g^{-1}, respectively (Fig. 5d). H-NiAl-LDH

3 electrode exhibits a significantly higher specific capacitance than that of P-NiAl-LDH

4 electrode at all current densities range, which is attributed to the nanoplates H-NiAl-

5 LDH possessing higher BET surface area that of the particle-typed P-NiAl-LDH, and

6 thus provides high electrochemical active sites for Faradaic reaction. With the increase

7 in current densities, the capacitance of the two samples decreases, which are caused by

8 the resistance of NiAl-LDH and the insufficient Faradaic redox reaction of the active

9 material under higher discharge current densities [28]. In addition, this outstanding

10 electrochemical performance of H-NiAl-LDH was higher than the previously reported,

11 such as Co-Al LDH-NS/GO (1031 F g^{-1} at 1 A g^{-1}) [39], NiCo cNW (1479 F g^{-1} at 1 A

12 g^{-1}) [40], CoFe LDH (456 F g^{-1} at 2 A g^{-1}) [41] and NiAl-LDH/CNFs (1613 F g^{-1} at 1

13 A g^{-1}) [42]. The cycling stability of the NiAl-LDH electrodes was further investigated

14 by galvanostatic charge/discharge cycling measurement (Fig. 5e). The P-NiAl-LDH

15 electrode exhibits a specific capacitance of 436.6 F g^{-1} (76.4% capacitance retention)

16 after 5000 cycles at the current density of 5 A g^{-1}, whereas the H-NiAl-LDH electrode

17 exhibits an impressive higher capacitance of 851.9 F g^{-1} (88.7% capacitance retention).

18 During the continuous prolong charge/discharge processes, the structure of LDH

19 suffered from considerable degradation, resulting in loss of capacitance [28, 30]. The

20 H-NiAl-LDH could maintain a good cycling stability is attributed to (1) high surface

21 area provides sufficient electrochemical active sites for redox reactions; (2) a thin

22 nanoplate structure can significantly ensure the fast ion diffusion by shortening the

23 diffusion paths, resulting in superior electrochemical performance of NiAl-LDH

1   nanoplates [43]; and (3) thin nanoplates preserve the distinctive structure integrity of

2   the materials during electrochemical reaction [44].

3

4   To understand the ion transport kinetics at the electrode/electrolyte interface, EIS was

5   carried out. Fig. 5f. Shows the impedance Nyquist plots of the samples. The proposed

6   equivalent circuit used for fitting the impedance curves is shown in the inset of Fig. 5f.

7   Results show the characteristic of quasi-semicircle in the high frequency region and

8   linear line in the low frequency region. At high frequency region, the intercept at real

9   axis (Z') is solution resistance (R_s), representing a combinational resistance of the

10 electrode, bulk electrolyte, and the resistance at the interface between the electrode

11 and active LDH materials. The R_s value of the H-NiAl-LDH electrode was 68%

12 smaller than that of the P-NiAl-LDH. The semicircle at high frequency region

13 represents the charge-transfer process at the working electrode-electrolyte interface

14 (R_{ct}), attributing from Faradaic reaction and the double layer capacitance (C_{dl}) on the

15 surface of the electrodes. The result showed that R_{ct} value of the H-NiAl-LDH

16 electrode was 97.8% smaller than that of the P-NiAl-LDH, indicating H-NiAl-LDH

17 possesses more electroactive surface area to provide short diffusion paths for ions and

18 electrons. In low frequency region, the straight line with an angle at almost 45° with

19 the real axis (Z') corresponds to the Warburg resistance (Z_w) and is the result of the

20 frequency dependence of ion diffusion in the electrolyte [45]. The impedance

21 parameters R_s, C_{dl}, R_{ct}, Z_w and C_F values calculated from the complex nonlinear least

22 square fitting are shown in Table 2. The C_{dl} value of H-NiAl-LDH electrode (4.68 mF)

23 was higher than that of P-NiAl-LDH electrode (2.3 mF), suggesting that nanoplate

24 structure of LDH is efficient in charge storage by adsorption. In addition, the W value

1 of the H-NiAl-LDH electrode (3.60 Ω s$^{-1/2}$) was 35% lower than that of the P-NiAl-

2 LDH electrode (5.54 Ω s$^{-1/2}$) and C_F value of the H-NiAl-LDH electrode (5.89 F) was

3 94.7% higher than that of P-NiAl-LDH (0.31 F), which further confirms that thin

4 nanoplate structure is a promising morphology to enhance the electrolyte transport in

5 electrode leading to enhanced electrochemical reactions.

6

7 The electrochemical performance of the graphene coated on Ni foam (G-NF) electrode

8 was explored in the three-electrode measurement using a 6 M KOH electrolyte (Fig.

9 6). The G-NF electrode exhibits a distinct rectangular shape at 5–50 mV s^{-1} scan rates,

10 revealing an excellent electrochemical performance at -1.0 ~ 0.0 V (vs. SCE) (Fig. 6a).

11 Fig. 6b shows that G-NF electrode exhibits symmetric galvanostatic charge/discharge

12 curves at different current density, indicating excellent reversibility of ion

13 absorption/desorption behavior [8, 46]. According to equation (2), the calculated

14 specific capacitance of G-NF electrode was 128 F g^{-1} at 1 A g^{-1} and retained 62.5% (80

15 F g^{-1}) of initial capacitance at 5 A g^{-1} (Fig. 6c), which is comparable to those reported

16 previously for graphene-based supercapacitors [47, 48]. EIS data showed that the R_s

17 and R_{ct} values of G-NF are 0.557 Ω and 0.678 Ω (Fig. 6d), respectively, indicating a

18 high conductivity nature and low charge transfer resistance of the G-NF electrode

19 owing to the large electroactive surface area of the graphene [49]. To evaluate the

20 performance of the H-NiAl-LD//G in SC applications, an ASC was fabricated using

21 as-prepared H-NiAl-LDH nanoplates and G-NF as the positive and negative

22 electrodes, respectively, with a piece of polypropylene paper as a separator in a 6 M

23 KOH solution. Based on the C_s values of the H-NiAl-LDH electrode and G-NF

24 electrode, as well as the principle of charge balance between the electrodes, the H-

15

1   NiAl-LDH to G-NF mass ratio was controlled at approximately 0.20 in the ASC. CV

2   curves of H-NiAl-LDH//G at different scan rates from 5 to 50 mV s^{-1}show the typical

3   characteristic of electric double-layer capacitance and pseudo-capacitance from 0 to

4   1.4 V without significant distortion of CV shape at high scan rate (Fig. 7a), indicating

5   high reversibility of the ASC device. The galvanostatic charge/discharge curves of H-

6   NiAl-LDH//G show good symmetrical at 1.4 V (Fig. 7b), revealing excellent

7   electrochemical reversibility and good Coulombic efficiency [50]. The high specific

8   capacitance of 125 F g^{-1} was recorded at 1 A g^{-1} and remained 82 F g^{-1} was 5 A g^{-1} in

9   H-NiAl-LDH//G (Fig. 7c). Remarkably, the ASC maintains an excellent cycling

10   stability with 91.8% of its initial capacitance retained after 5000 cycles at 5 A g^{-1} (Fig.

11   7d). Based on these C_s values, the highest energy density of the asymmetric

12   supercapacitor (Fig. 7e) was calculated to be 34.1 Wh kg^{-1} at a power density of 700

13   W kg^{-1}. The results show that the ASC achieved a higher energy density than the other

14   devices, such as Ni(OH)$_2$@3D Ni//AC (21.8 Wh kg^{-1} at 660 W kg^{-1}) [50], NiCo LDH-

15   ZTO//AC (23.7 Wh kg^{-1} at 284.2 W kg^{-1}) [51], NiCo oxide//AC (7.4 Wh kg^{-1} at 1900

16   W kg^{-1}) [52], NiCo$_2$O$_4$-rGO//AC (23.3 Wh kg^{-1} at 324.9 W kg^{-1}) [53] and LDH-

17   NF/GNS//GNS-NF (31.5 Wh kg^{-1} at 400 W kg^{-1}) [54]. To further demonstrate the

18   practical application of H-NiAl-LDH//G ASC, two ASCs were connected in series to

19   power a red light-emitting diode (Fig. 7f).

20

21   **Conclusions**

22   In conclusion, NiAl-LDH nanoplates had been fabricated through a facile

23   hydrothermal method. The as-fabricated H-NiAl-LDH electrode exhibits excellent

24   supercapacitor performance with a specific capacitance of 1713.2 F g^{-1} at 1 A g^{-1} and

1   remarkable cycling stability compared to the particle-typed P-NiAl-LDH material. The

2   thin thickness (~30 nm) of LDH nanoplate features account for the impressive

3   electrochemical performance. Furthermore, the ASC based on H-NiAl-LDH and

4   graphene as positive and negative electrodes, respectively, in 6 M KOH aqueous

5   electrolyte delivers high specific energy and power densities as well as excellent

6   cycling stability. This work provides a facile method to synthesize nanoplated LDH

7   electrode materials for high-performance supercapacitors.

8

12

13

14

15

16

17

18

19

20

21

22

23

24

1

2

3

4

References

[1] C. Yuan, H.B. Wu, Y. Xie, X.W.D. Lou, Angew. Chem. Int. Ed., 53 (2014) 1488.

[2] J. Yang, C. Yu, X. Fan, J. Qiu, Adv. Energy Mater., 4 (2014) 1400761.

[3] M. Winter, R.J. Brodd, Chem. Rev., 104 (2004) 4245-4269.

[4] J.R. Miller, P. Simon, Science, 321 (2008) 651-652.

[5] H.Y. Chen, F. Cai, Y.R. Kang, S. Zeng, M.H. Chen, Q.W. Li, ACS Appl. Mater. Interfaces, 6 (2014) 19630-19637.

[6] L.J. Zhang, J. Wang, J.J. Zhu, X.G. Zhang, K.S. Hui, K.N. Hui, J. Mater. Chem. A, 1 (2013) 9046-9053.

[7] X.J. Li, Y. Zhang, W. Xing, L. Li, Q.Z. Xue, Z.F. Yan, J. Power Sources, 331 (2016) 67-75.

[8] Q.B. Zhang, B.T. Zhao, J.X. Wang, C. Qu, H.B. Sun, K.L. Zhang, M.L. Liu, Nano Energy, 28 (2016) 475-485.

[9] M.F. Shao, R.K. Zhang, Z.H. Li, M. Wei, D.G. Evans, X. Duan, Chem. Commun., 51 (2015) 15880-15893.

[10] J. Xu, F. He, S.L. Gai, S.H. Zhang, L. Li, P.P. Yang, Nanoscale, 6 (2014) 10887-10895.

[11] Y.Q. Zhu, C.B. Cao, S. Tao, W.S. Chu, Z.Y. Wu, Y.D. Li, Sci. Rep., 4 (2014) 5787.

[12] F. Ning, M. Shao, C. Zhang, S. Xu, M. Wei, X. Duan, Nano Energy, 7 (2014) 134-142.

[13] L. Zhang, K.N. Hui, K. San Hui, H. Lee, J. Power Sources, 318 (2016) 76-85.

[14] J. Yan, Z.J. Fan, W. Sun, G.Q. Ning, T. Wei, Q. Zhang, R.F. Zhang, L.J. Zhi, F. Wei, Adv. Funct. Mater., 22 (2012) 2632-2641.

[15] G.H. Cheng, W.F. Yang, C.Q. Dong, T.Y. Kou, Q.G. Bai, H. Wang, Z.H. Zhang, J. Mater. Chem. A, 3 (2015) 17469-17478.

[16] K. Liang, X.Z. Tang, B.Q. Wei, W.C. Hu, Mater. Res. Bull., 48 (2013) 3829-3833.

[17] Q. Yang, Z.Y. Lu, X.M. Sun, J.F. Liu, Sci. Rep., 3 (2013) 3537.

[18] C.Z. Yuan, J.Y. Li, L.R. Hou, X.G. Zhang, L.F. Shen, X.W. Lou, Adv. Funct. Mater., 22 (2012) 4592-4597.

[19] K. Liang, N. Wang, M. Zhou, Z.Y. Cao, T.L. Gu, Q. Zhang, X.Z. Tang, W.C. Hu, B.Q. Wei, J. Mater. Chem. A, 1 (2013) 9730-9736.

[20] L. Yan, R. Li, Z. Li, J. Liu, Y. Fang, G. Wang, Z. Gu, Electrochim. Acta, 95 (2013) 146-154.

[21] L.J. Zhang, X.G. Zhang, L.F. Shen, B. Gao, L. Hao, X.J. Lu, F. Zhang, B. Ding, C.Z. Yuan, J. Power Sources, 199 (2012) 395-401.

[22] J.P. Cheng, J.H. Fang, M. Li, W.F. Zhang, F. Liu, X.B. Zhang, Electrochim. Acta, 114 (2013) 68-75.

[23] H. Chen, L.F. Hu, M. Chen, Y. Yan, L.M. Wu, Adv. Funct. Mater., 24 (2014) 934-942.

[24] X. Bai, Q. Liu, H.S. Zhang, J.Y. Liu, Z.S. Li, X.Y. Jing, Y. Yuan, L.H. Liu, J. Wang, Electrochim. Acta, 215 (2016) 492-499.

[25] J.W. Zhao, J. Chen, S.M. Xu, M.F. Shao, Q. Zhang, F. Wei, J. Ma, M. Wei, D.G. Evans, X. Duan, Adv. Funct. Mater., 24 (2014) 2938-2946.

[26] J. Wu, W.W. Liu, Y.X. Wu, T.C. Wei, D.S. Geng, J. Mei, H. Liu, W.M. Lau, L.M. Liu, Electrochim. Acta, 203 (2016) 21-29.

[27] G.P. Xiong, P.G. He, D.N. Wang, Q.Q. Zhang, T.F. Chen, T.S. Fisher, Adv. Funct. Mater., 26 (2016) 5460-5470.

[28] L. Zhang, K.N. Hui, K.S. Hui, H. Lee, Electrochim. Acta, 186 (2015) 522-529.

[29] J. Yang, C. Yu, X.M. Fan, J.S. Qiu, Adv. Energy Mater., 4 (2014) 1400761.

[30] X.M. Li, J.T. Zai, Y.Y. Liu, X.B. He, S.J. Xiang, Z.F. Ma, X.F. Qian, J. Power Sources, 325 (2016) 675-681.

[31] F.Z. Zhang, L. Guo, S.L. Xu, R. Zhang, Langmuir, 31 (2015) 6704-6712.

1 [32] J.H. Fang, M. Li, Q.Q. Li, W.F. Zhang, Q.L. Shou, F. Liu, X.B. Zhang, J.P. Cheng,

2 Electrochim. Acta, 85 (2012) 248-255.

3 [33] B. Wang, G.R. Williams, Z. Chang, M.H. Jiang, J.F. Liu, X.D. Lei, X.M. Sun, ACS Appl.

4 Mater. Interfaces, 6 (2014) 16304-16311.

5 [34] J. Yang, C. Yu, X.M. Fan, Z. Ling, J.S. Qiu, Y. Gogotsi, J. Mater. Chem. A, 1 (2013)

6 1963-1968.

7 [35] D.P. Dubal, P. Gomez-Romero, B.R. Sankapal, R. Holze, Nano Energy, 11 (2015) 377.

8 [36] M.Q. Zhao, Q. Zhang, J.Q. Huang, F. Wei, Adv. Funct. Mater., 22 (2012) 675-694.

9 [37] S.K. Meher, P. Justin, G. Ranga Rao, ACS Appl. Mater. Interfaces, 3 (2011) 2063-2073.

10 [38] Y.F. Zhao, Q. Wang, T. Bian, H.J. Yu, H. Fan, C. Zhou, L.Z. Wu, C.H. Tung, D. O'Hare,

11 T.R. Zhang, Nanoscale, 7 (2015) 7168-7173.

12 [39] L. Wang, D. Wang, X.Y. Dong, Z.J. Zhang, X.F. Pei, X.J. Chen, B.A. Chen, J.A. Jin,

13 Chem. Commun., 47 (2011) 3556-3558.

14 [40] X. Wang, C.Y. Yan, A. Sumboja, P.S. Lee, Nano Energy, 3 (2014) 119-126.

15 [41] X. Ge, C.D. Gu, X.L. Wang, J.P. Tu, J. Mater. Chem. A, 2 (2014) 17066-17076.

16 [42] F. He, Z.B. Hu, K.Y. Liu, S.R. Zhang, H.T. Liu, S.B. Sang, J. Power Sources, 267 (2014)

17 188-196.

18 [43] S.X. Wu, K.S. Hui, K.N. Hui, K.H. Kim, J. Mater. Chem. A, 4 (2016) 9113-9123.

19 [44] S. Liu, K.S. Hui, K.N. Hui, J.M. Yun, K.H. Kim, J. Mater. Chem. A, 4 (2016) 8061-8071.

20 [45] M.D. Stoller, S.J. Park, Y.W. Zhu, J.H. An, R.S. Ruoff, Nano Lett., 8 (2008) 3498-3502.

21 [46] K.S. Hui, K.N. Hui, D.A. Dinh, C.H. Tsang, Y.R. Cho, W. Zhou, X.T. Hong, H.H. Chun,

22 Acta Mater., 64 (2014) 326-332.

23 [47] Z.S. Wu, A. Winter, L. Chen, Y. Sun, A. Turchanin, X.L. Feng, K. Mullen, Adv. Mater.,

24 24 (2012) 5130-5135.

1 [48] J.C. Huang, P.P. Xu, D.X. Cao, X.B. Zhou, S.N. Yang, Y.J. Li, G.L. Wang, J. Power

2 Sources, 246 (2014) 371-376.

3 [49] M.S. Wu, M.J. Wang, J.J. Jow, J. Power Sources, 195 (2010) 3950-3955.

4 [50] Y.Z. Su, K. Xiao, N. Li, Z.Q. Liu, S.Z. Qiao, J. Mater. Chem. A, 2 (2014) 13845-13853.

5 [51] X. Wang, A. Sumboja, M.F. Lin, J. Yan, P.S. Lee, Nanoscale, 4 (2012) 7266-7272.

6 [52] C.H. Tang, Z. Tang, H. Gong, J. Electrochem. Soc., 159 (2012) A651-A656.

7 [53] X. Wang, W.S. Liu, X.H. Lu, P.S. Lee, J. Mater. Chem., 22 (2012) 23114-23119.

8 [54] L.J. Zhang, K.N. Hui, K.S. Hui, X. Chen, R. Chen, H.W. Lee, Int. J. Hydrogen Energ.,

9 41 (2016) 9443-9453.

10

11

12

13

14

15

16

17

18

19

20

21

22

23

24

1   **Fig. 1**

2
3
4

5
6
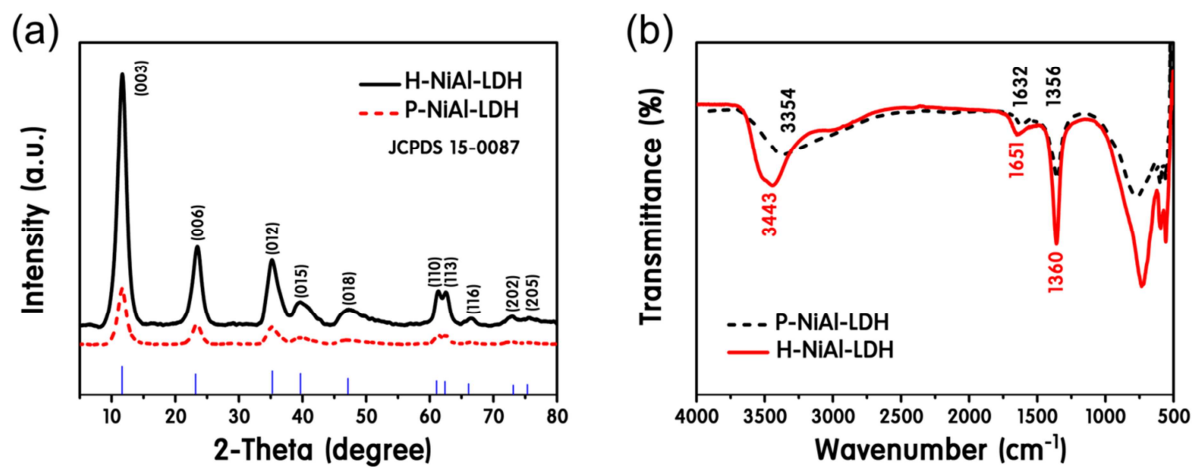
7   Fig. 1. XRD patterns (a) and FT-IR spectra (b) of P-NiAl-LDH and H-NiAl-LDH.

8
9
10
11
12
13
14
15
16
17
18
19
20
21
22
23
24
25
26
27
28
29
30
31
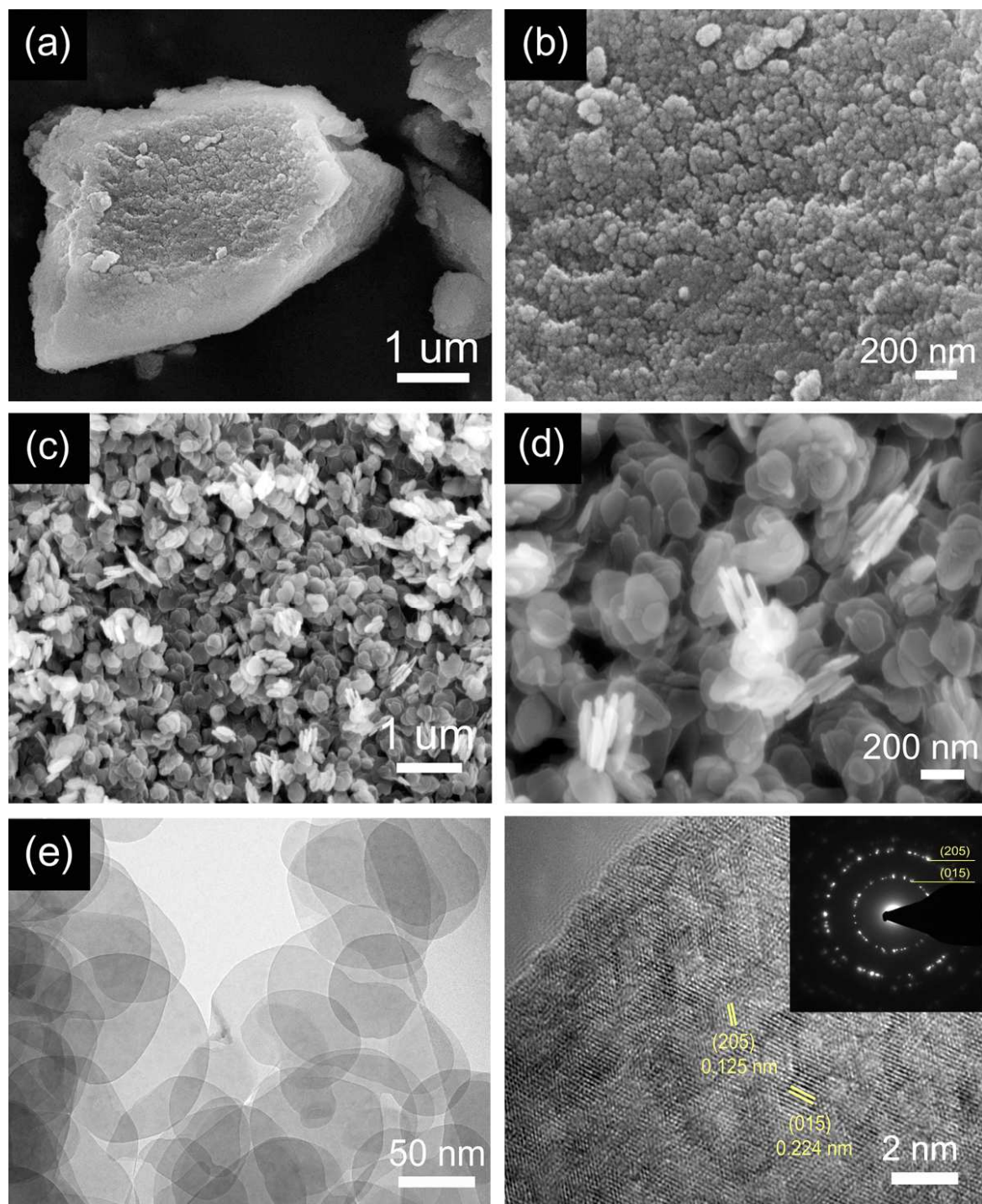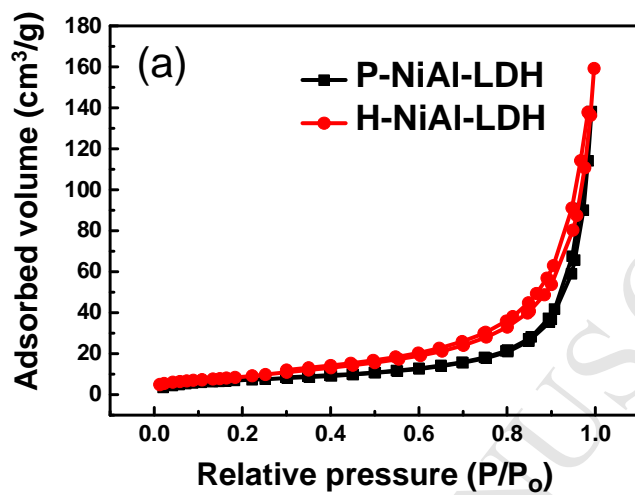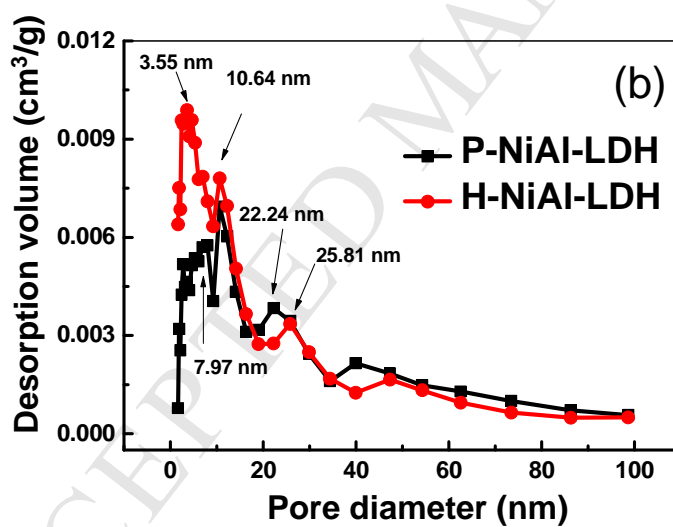32
33
34
35
36
37
38
39

1 **Fig. 2**

2

3
4
5 Fig. 2. SEM images of the P-NiAl-LDH (a and b) and H-NiAl-LDH (c and d). TEM (e) and

6 HRTEM (f) images of the H-NiAl-LDH. Inset of (f) shows the SAED pattern of H-NiAl-

7 LDH.

1

2

3 **Fig. 3**

4

5

6
7
8
9
10 Fig. 3. (a) N_2 adsorption-desorption isotherm loop and (b) pore size distribution data of P-

11 NiAl-LDH and H-NiAl-LDH.

12
13
14
15
16
17
18

25

1

2

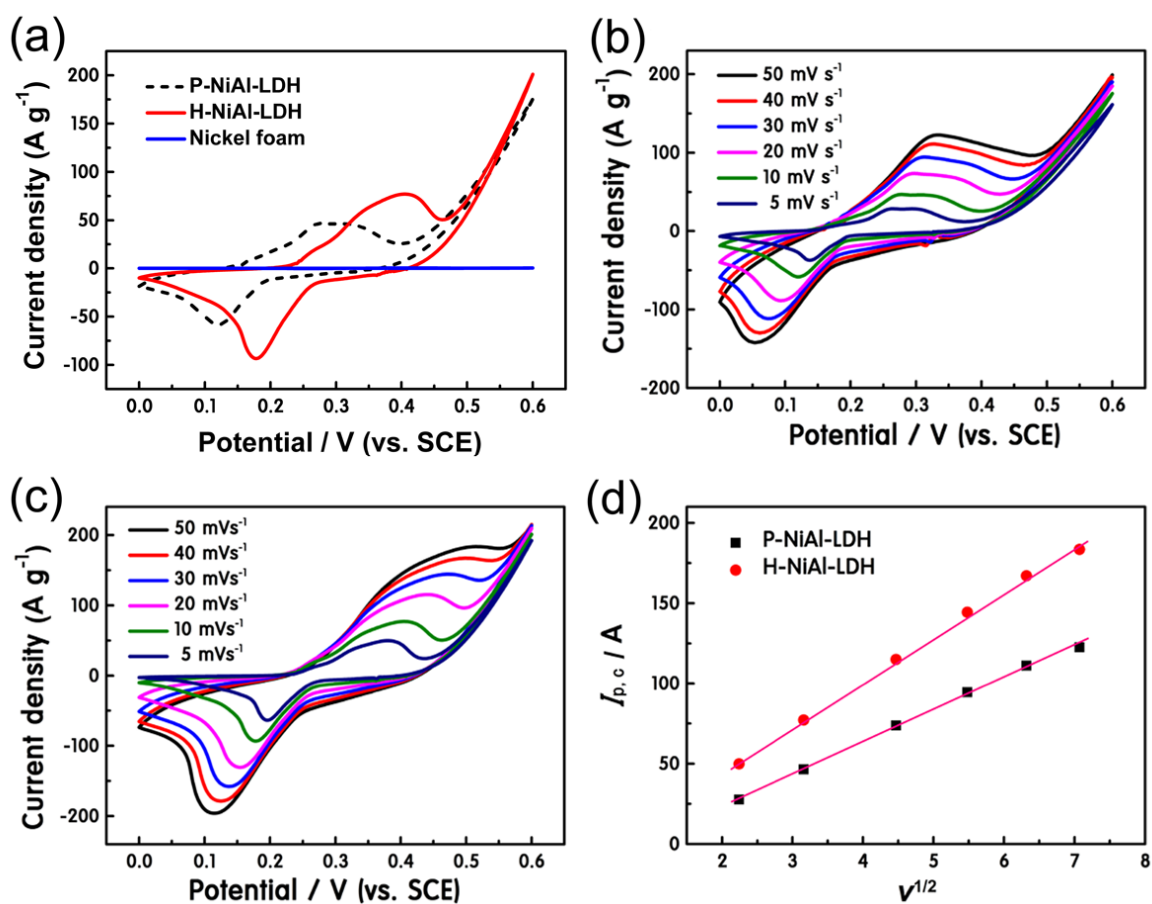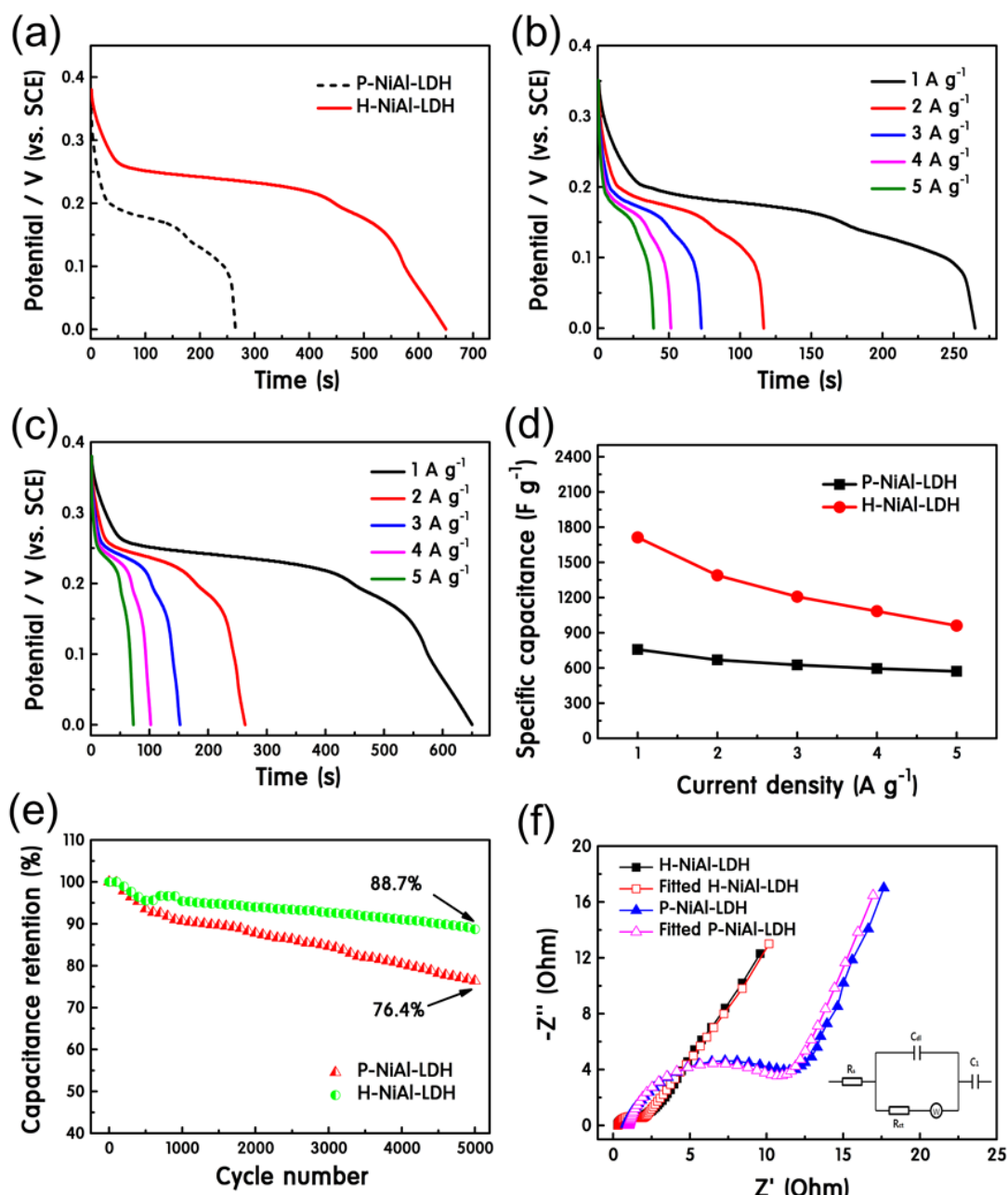1   **Fig. 4**

2
3

4
5
6   Fig. 4. CV curves of (a) nickel foam, P-NiAl-LDH and H-NiAl-LDH electrodes

7   measured in a 6.0 M KOH at scan rate of 10 mV s^{-1}. CV curves of (b) P-NiAl-LDH and (c)

8   H-NiAl-LDH electrodes measured in a 6.0 M KOH at various scan rates (5-50 mV s^{-1}). (d)

9   Plots of the cathodic peak current densities obtained from (b, c) versus the square root of scan

10   rates.

11

12
13
14
15
16
17
18
19
20

1
2
3

1   **Fig. 5**

2
3
4
5   Fig. 5. Galvanostatic charge/discharge curves of (a) P-NiAl-LDH and H-NiAl-LDH

6   electrodes at a current density of 1 A g^{-1}, and (b) P-NiAl-LDH and (c) H-NiAl-LDH

7   electrodes at different current densities. (d) Specific capacitances of the P-NiAl-LDH

8   and H-NiAl-LDH electrodes measured at various current densities ranging from 1 A

9   g^{-1} to 5 A g^{-1}. (e) Capacitance retentions and (f) Nyquist plots of the P-NiAl-LDH and

10   H-NiAl-LDH electrodes. (bottom-right inset is the fitted circuit of Nyquist plot).
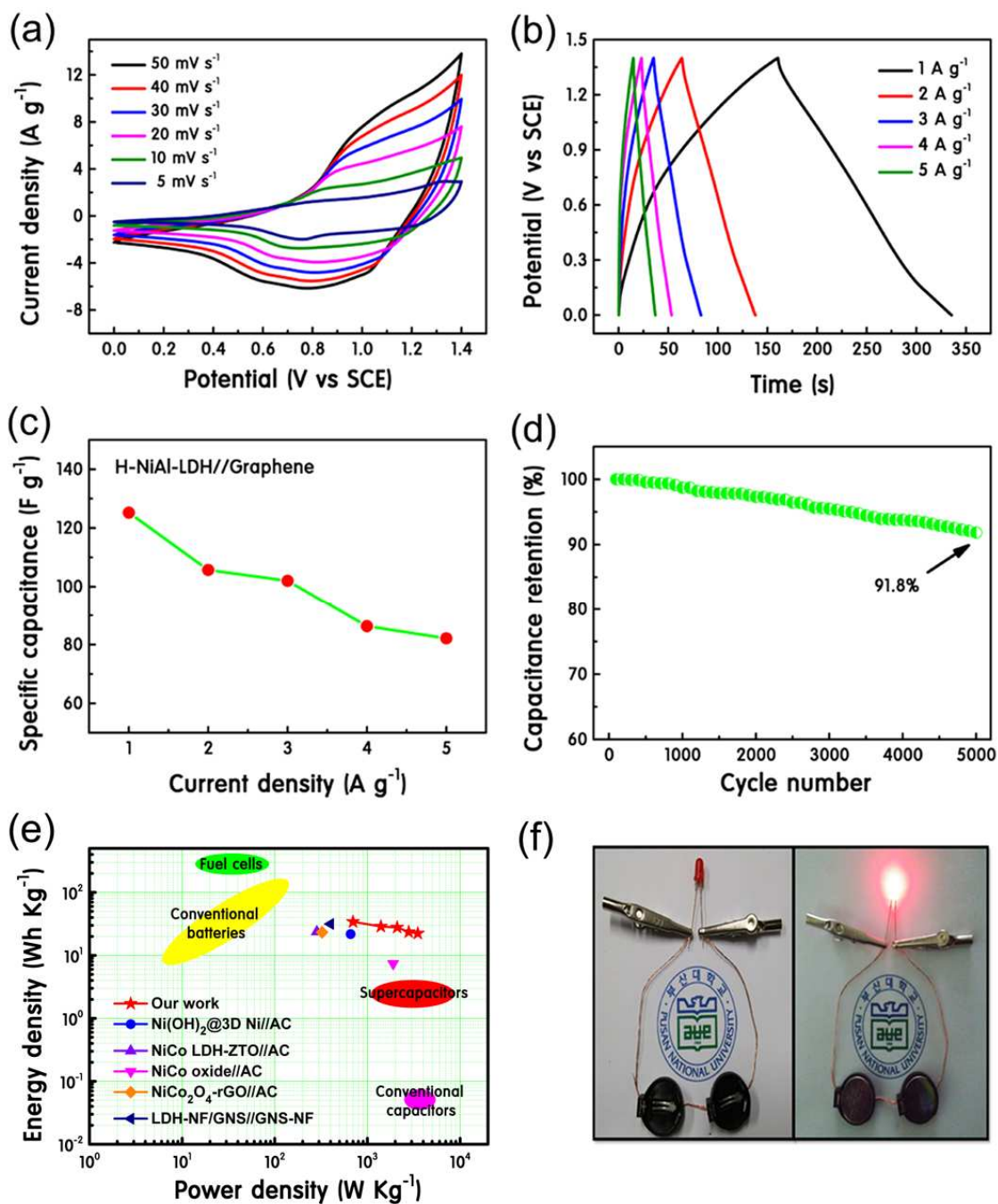
11

1 **Fig. 6**
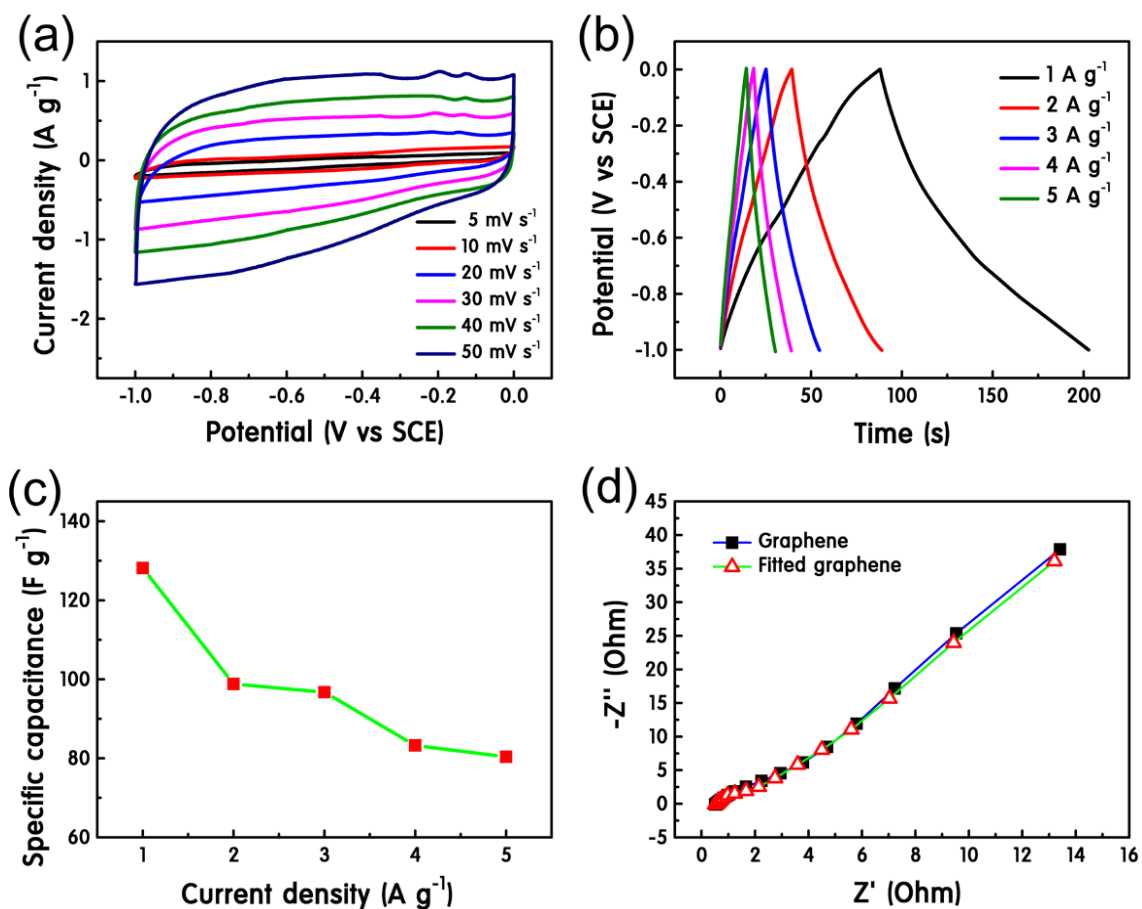
2
3
4

5 Fig. 6. (a) CV curves of the graphene electrode at different scan rates. (b) Galvanostatic

6 charge/discharge curves of graphene electrode. (c) Specific capacitance of graphene electrode

7 at different current densities. (d) Nyquist plot of graphene electrode.

8
9
10
11
12
13
14
15
16
17
18
19
20
21
22

1 **Fig. 7**

2
3
4 Fig. 7. (a) CV curves of H-NiAl-LDH//graphene ASC at different scan rates; (b)
5 Galvanostatic charge/discharge curves of H-NiAl-LDH//graphene ASC. (c) Specific
6 capacitance and (d) cycling performance of H-NiAl-LDH//graphene ASC. (e) Ragone plots
7 of the H-NiAl-LDH//graphene ASC compared to the references. (f) The digital photo of two
8 H-NiAl-LDH//graphene ASCs lighting up a red LED.

Table 1 Specific surface area, pore volume, and pore size of P-NiAl-LDH and H-NiAl-L

DH electrodes.

Samples	S_{BET} (m^2 g^{-1})	V_{Pores} (cm^3 g^{-1})	Pore size (nm)
P-NiAl-LDH	26.54	0.20	10.64
H-NiAl-LDH	31.35	0.23	3.55

1

2 **Table 2** Impedance parameters obtained from the equivalent circuit of P-NiAl-LDH and H-

3 NiAl-LDH electrodes.

4
5

	R_s (Ω)	R_{ct} (Ω)	C_{dl} (F)	W (Ωs$^{-1/2}$)	C_F (F)
P-NiAl-LDH	1.019	0.00223	13.529	5.544	0.314
H-NiAl-LDH	0.327	0.00468	0.289	3.601	5.891

6
7

8

9

10

11
12

Highlights

- 2D NiAl layered double hydroxide nanoplates was synthesized by hydrothermal method.
- 2D NiAl LDH electrode delivered high specific capacitance of 1713.2 F g^{-1} at 1 A g^{-1}.
- Asymmetric supercapacitor delivered a high energy density of 34.1 Wh kg^{-1}.
- Outstanding cyclic stability of 91.8% capacitance retention after 5000 cycles was achieved.